Solar Physics (2006) 235: 161–190
DOI: 10.1007/s11207-006-0068-7

NONLINEAR FORCE-FREE MODELING OF CORONAL MAGNETIC FIELDS PART I: A QUANTITATIVE COMPARISON OF METHODS

CAROLUS J. SCHRIJVER, MARC L. DEROSA, and THOMAS R. METCALF
Lockheed Martin Advanced Technology Center, Palo Alto, California, U.S.A.
(e-mails: schryver@lmsal.com; derosa@lmsal.com; metcalf@lmsal.com)

YANG LIU
Stanford University (HEPL), Stanford, California, U.S.A.
(e-mail: yliu@quake.stanford.edu)

JIM MCTIERNAN
Space Sciences Laboratory, University of California, Berkeley, California, U.S.A.
(e-mail: jimm@ssl.berkeley.edu)

STÉPHANE RÉGNIER
European Space Agency, RSSD/ESTEC, Noordwijk, The Netherlands
(e-mail: sregnier@rssd.esa.int)

GHERARDO VALORI
Astrophysical Institute Potsdam, Germany
(e-mail: gvalori@aip.de)

MICHAEL S. WHEATLAND
School of Physics, University of Sydney, New South Wales, Australia
(e-mail: wheatland@physics.usyd.edu.au)

and

THOMAS WIEGELMANN
Max Planck Institut für Sonnensystemforschung, Katlenburg-Lindau, Germany
(e-mail: wiegelmann@linmpi.mpg.de)

(Received 13 September 2005; accepted 19 December 2005)

Abstract. We compare six algorithms for the computation of nonlinear force-free (NLFF) magnetic fields (including optimization, magnetofrictional, Grad–Rubin based, and Green's function-based methods) by evaluating their performance in blind tests on analytical force-free-field models for which boundary conditions are specified either for the entire surface area of a cubic volume or for an extended lower boundary only. Figures of merit are used to compare the input vector field to the resulting model fields. Based on these merit functions, we argue that all algorithms yield NLFF fields that agree best with the input field in the lower central region of the volume, where the field and electrical currents are strongest and the effects of boundary conditions weakest. The NLFF vector fields in the outer domains of the volume depend sensitively on the details of the specified boundary conditions; best agreement is found if the field outside of the model volume is incorporated as part of the model boundary, either as potential field boundaries on the side and top surfaces, or as a potential field in a skirt around the main volume of interest. For input field (**B**) and modeled field (**b**), the best method included in our study yields an average relative vector error $E_{\mathrm{n}} = \langle |\mathbf{B}-\mathbf{b}| \rangle / \langle |\mathbf{B}| \rangle$ of only 0.02 when all sides are specified and 0.14 for the case where only the lower boundary is specified, while

the total energy in the magnetic field is approximated to within 2%. The models converge towards the central, strong input field at speeds that differ by a factor of one million per iteration step. The fastest-converging, best-performing model for these analytical test cases is the Wheatland, Sturrock, and Roumeliotis (2000) optimization algorithm as implemented by Wiegelmann (2004).

1. Introduction

The geometry and dynamics of the solar corona are determined by the evolving electromagnetic field at the Sun's surface. The coronal extension of the magnetic field and the electrical currents that it carries determine the confining forces for the multitude of plasma atmospheres that emit predominantly X-ray and EUV radiation. The energy in the electrical currents may at times be (partially) released in impulsive solar flares, in eruptive coronal mass ejections, or most commonly in gradual rearrangements of the magnetic field and in the plasma volumes that it contains.

Understanding the coronal electromagnetic field is a complex problem because of both intrinsic physical problems and observational limitations. On the observational side, we face the problem that we cannot measure the magnetic field reliably in enough of the solar outer atmosphere to compare models directly to observations. This problem will likely persist for a considerable time, because even if we succeed in learning to employ coronal diagnostics to measure the magnetic field, the line-of-sight integration in optically thin (X-ray and EUV) radiation and the lack of a height scale for optically thick (radio) radiation will preclude the unambiguous determination of the spatially resolved vector-magnetic field in the solar corona.

The only environment for which we can currently measure the vector magnetic field is the photosphere of the Sun. Even there the measurement is subject to substantial observational noise and modeling biases which complicate the inversion of the polarization signals. Moreover, there is an intrinsic 180° ambiguity in the direction of the vector components perpendicular to the line of sight (*e.g.*, Metcalf, 1994). In these relatively dense layers of the solar atmosphere, the plasma forces are still considerable compared to the magnetic forces. Extrapolating the measured photospheric vector field into the solar corona consequently requires knowledge of the plasma forces that act on that magnetic field at least throughout the upper photospheric and chromospheric domains.

In the corona, the lack of observational constraints for the magnetic field is alleviated by the fact that much of the time, most of the coronal field is not affected by the plasma that it carries. The coronal field is therefore often said to be "force-free," *i.e.*, free of forces other than the balancing electromagnetic forces that it exerts on itself (but see, *e.g.*, Gary, 2001).

Even the simplification that the coronal field is force free does not solve all our problems, however, because we have – at least at present – inadequate access to the upper chromospheric field from where the forces of the field are generally assumed

to dominate those of the plasma (Metcalf *et al.*, 1995). Hence the observable photospheric vector field needs to be extrapolated through the non-force-free environment of the upper photosphere and lower chromosphere, which is a problem that remains to be solved.

Moreover, the computation of a force-free field itself is subject to numerical instabilities that require considerable attention. On top of all this, the nonlinearity of the problem makes it unavoidable that the results are highly sensitive to even relatively distant fields or – in case a partial coronal volume is computed – on how much is known about the boundary conditions at the edges of the model volume.

As a consequence of these problems, many quantitative studies of the solar coronal field continue to use the simplest of the force-free fields, namely the current-free potential field. Such models, although often fairly good approximations (*e.g.*, Schrijver *et al.*, 2005), cannot be used to determine the energy contained in electrical currents and magnetic fields available for driving instabilities, or even provide the simple assessment of where such energy might exist within active regions.

Potential fields are often not suitable to describe the magnetic field topology in active regions. The next level of model is the so-called linear force-free-field model, which assumes a fixed ratio (α) between electrical current density and magnetic field strength throughout the corona. Whereas this often provides a fair approximation to the coronal field over active regions, the unphysical assumption of a constant α precludes the measurement of the available, or free, energy in the corona (in fact, it results in a formally unbounded energy if applied to the entire volume above the solar surface, *e.g.*, Seehafer, 1978).

Several methods have been developed over the past few decades to compute the most general class of force-free fields, the so-called nonlinear force-free (NLFF) field (described in Sections 2 and 3). This class of field configuration is difficult to compute, and solutions depend strongly on the implementation of the boundaries.

The study described in this paper is part of a project that aims to evaluate and address these problems, with the ultimate goal of developing a fast, reliable method of measuring coronal free energy in active regions. We focus here on a quantitative assessment of several existing NLFF field modeling methods by applying them first to known analytical test cases, to later evaluate their results when applied to vector magnetic field measurements of solar active regions. We also discuss the effects of different methods of applying boundary and initial conditions, and evaluate required computing times and scalings with grid sizes.

2. Some Properties of Force-Free Fields

Force-free coronal magnetic fields are defined entirely by requiring that the field has no Lorentz force and is divergence free (the "solenoidal condition"):

$$\mu_0 \mathbf{J} \times \mathbf{B} = (\nabla \times \mathbf{B}) \times \mathbf{B} \equiv 0, \tag{1}$$

$$\nabla \cdot \mathbf{B} \equiv 0, \tag{2}$$

where **B** and **J** are the vectors of the magnetic field strength and of the electrical current density. Equation (1) can be rewritten by introducing a scalar function (α), sometimes known as the torsion function, so that

$$\mu_0 \mathbf{J} = \nabla \times \mathbf{B} = \alpha \mathbf{B}, \tag{3}$$

$$\mathbf{B} \cdot \nabla \alpha = 0, \tag{4}$$

where Equation (4), which results by taking the divergence of Equation (3) and using Equation (2), shows that α is constant along field lines for any NLFF field.

For $\alpha = 0$ the above equations describe a potential field, which is both force-free and current-free. For $\alpha =$ constant, they describe a current-carrying linear force-free (LFF) field, and for $\alpha = f(\mathbf{r})$ a general nonlinear force-free field (referred to below as a NLFF field), depending on position ($\mathbf{r}$).

The modeling of a NLFF field is, not surprisingly, sensitive to the boundary conditions. Some insight into this can be gained directly from Equation (4): as there can be no gradient in α along individual magnetic field lines, all field lines that intersect the photosphere on both ends, must end on locations with the same value of α, *i.e.*, with the same ratio and relative direction between field strength and current density.

Equation (3) indicates that the value of α at the photospheric boundary specified by a vector field measurement with horizontal components B_x and B_y and vertical component B_z is given by

$$\alpha = \frac{1}{B_z}\left(\frac{\partial B_y}{\partial x} - \frac{\partial B_x}{\partial y}\right). \tag{5}$$

In other words, the photospheric vector field uniquely defines the map of α for the lower boundary condition (disregarding the non-force-free nature of the photosphere for a moment). As field lines must connect pairs of points $(x_{1,2}, y_{1,2})$ with $\alpha(x_1, y_1) = \alpha(x_2, y_2)$, the connectivity that is to be established by the NLFF field modeling is strongly constrained by that map. Low and Lou (1990) illustrate the consequences of measurement noise for this connectivity problem by pointing out the particular case of a field line that connects the absolute minima in α on the lower (photospheric) boundary: if α at one of the footpoints of that field line is increased by the measurement errors, then the problem becomes formally unsolvable. We note that in practice, this problem is commonly avoided – not solved – by applying the α field only in one polarity of the vector magnetic field at the lower boundary.

This same problem for the field solution shows up equally forcefully when we realize that vector fields are measured for only a small part of the solar surface. Such measurements are often available only for a field of view that does not contain an entire active region or is generally not flux balanced, while coronal observations readily show that active regions are generally connected to distant field either in other active regions or in the surrounding quiet Sun (see, *e.g.*, TRACE images

in Schrijver *et al.*, 1999). Imposing flux balance, or requiring all field lines to close within the computational volume unavoidably affects the connectivity of the field, and that in turn affects the field structure and the free energy contained within it.

The mathematical difficulties that these problems pose are often circumvented by restricting the information used from the vector magnetic field measurement to, for example, the normal component of the field, B_z, and α for only one polarity of the field (see the discussion by Wheatland, Sturrock, and Roumeliotis, 2000). But removing a mathematical difficulty is not the same as addressing the physical problem: we ultimately need to find a modeling approach that allows for the fact that the vector magnetic field in the photosphere is really only an approximate boundary condition.

2.1. LOW–LOU MODEL

Low and Lou (1990) describe a special class of NLFF fields for which Equations (1) and (2) can be written as a second-order partial differential equation (with eigenvalues m_{LL} and n_{LL}). These fields are axially symmetric, but Low and Lou (1990) show that arbitrary positioning of a plane (characterized by the parameters ℓ and Φ) within these solutions to represent the Sun's surface under active region fields can provide boundary conditions and overlying fields that are useful as test cases for NLFF field modeling algorithms. We use two of these solutions as test cases:

Case I: $n_{\mathrm{LL}} = 1$, $m_{\mathrm{LL}} = 1$, $\ell = 0.3$, $\Phi = \pi/4$. The vector field on all six boundaries of a 64^3-pixel cubic volume bounded by $x, y \in [-1, +1]$ and $z \in [0, 2]$ was provided, with the aim of determining the NLFF field in this volume. This input field is shown in Figure 4 of Low and Lou (1990) and was used by Wheatland, Sturrock, and Roumeliotis (2000) as a test case in the development of the optimization method. The vector field for all six boundaries of a cubic volume is specified for Case I on a 64×64 grid.

Case II: $n_{\mathrm{LL}} = 3, m_{\mathrm{LL}} = 1, \ell = 0.3, \Phi = 4\pi/5$. The vector field on only the surface bounded by $x, y \in [-3, +3]$ was provided. The surface vector field is specified as the boundary condition for Case II on a 192×192 pixel grid centered on the 64^3-pixel test region.

These fields are shown in panels *a* of Figures 1–4. Case I is significantly more non-potential over a greater fraction of the model volume than Case II, even as Case II is more non-potential near the center of the model region (compare also the field energies contained in the model volume listed in Tables I and II). The region of strongest field is more compact in Case II than in Case I in order to reduce the relative sensitivity to the unspecified "far field" in Case II, as described in Section 5.1.

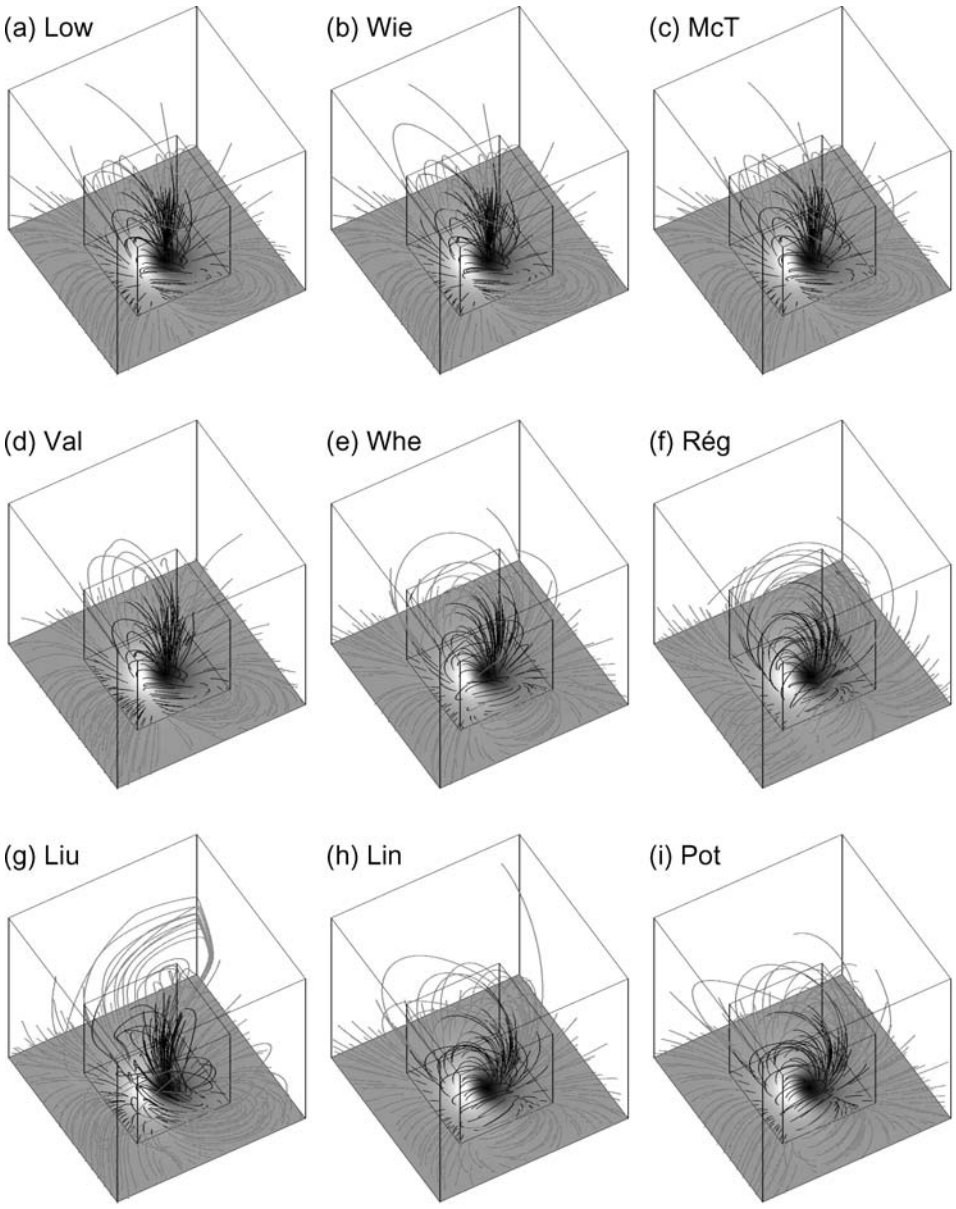

Figure 1. Magnetic fields for Case I in which all six side boundaries were provided to the modelers. The field lines were started from a regular rectangular grid. The field lines within the inner half of the model volume (as outlined by the smaller cube) are shown in black. The field in the inner volume is shown enlarged in Figure 2. The panels are in the same order as the entries in Table I: (a) Low and Lou input model; (b) Wiegelmann; (c) McTiernan; (d) Valori; (e) Wheatland; (f) Régnier; (g) Liu; (h) LFF field; (i) potential field.

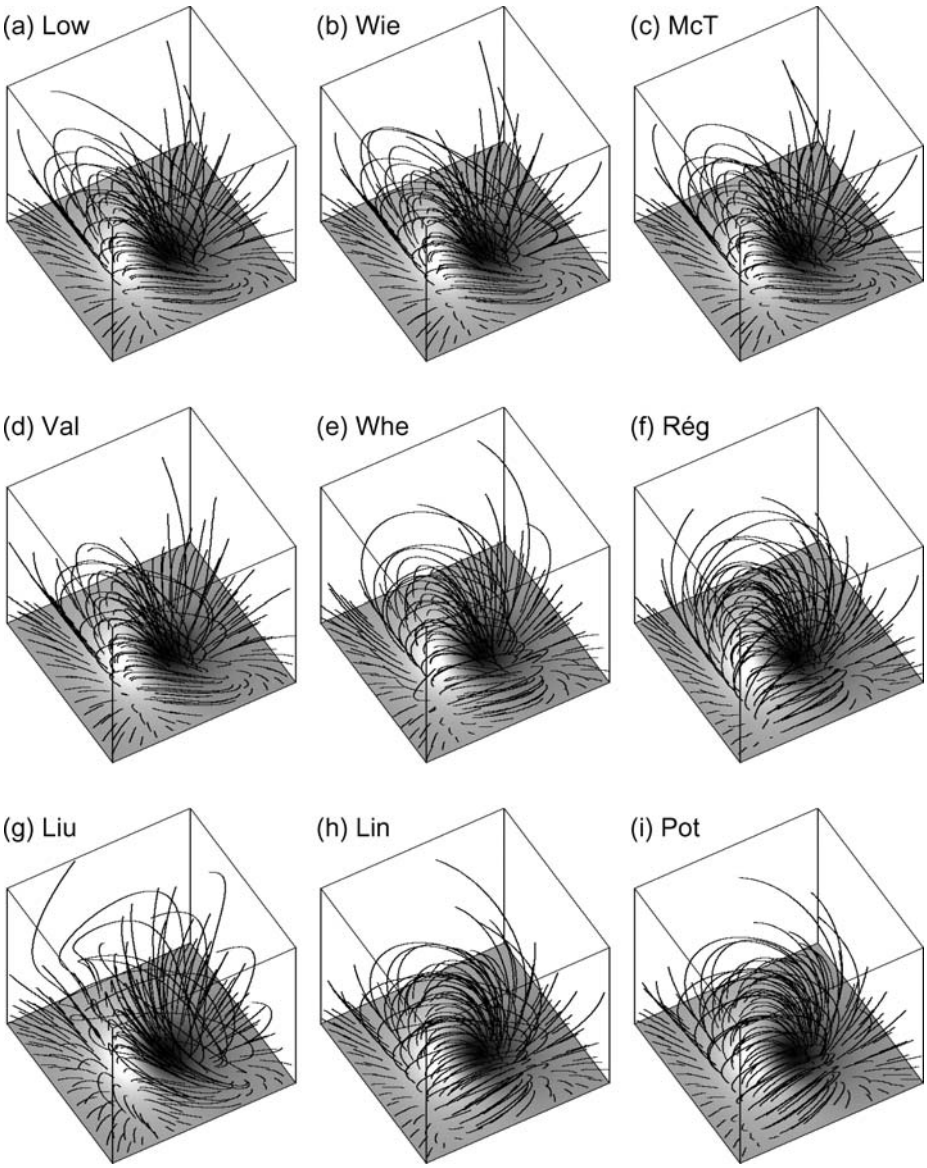

Figure 2. As Figure 1, but showing only the central domain of the model volume, as outlined by the small cube in Figure 1. Note that more field lines are drawn in this figure than in Figure 1.

3. Description of Methods

3.1. Potential and linear force-free fields

The linear force-free field was computed using the Fourier method described by Gary (1989) with the vertical Low and Lou field as the boundary condition. The

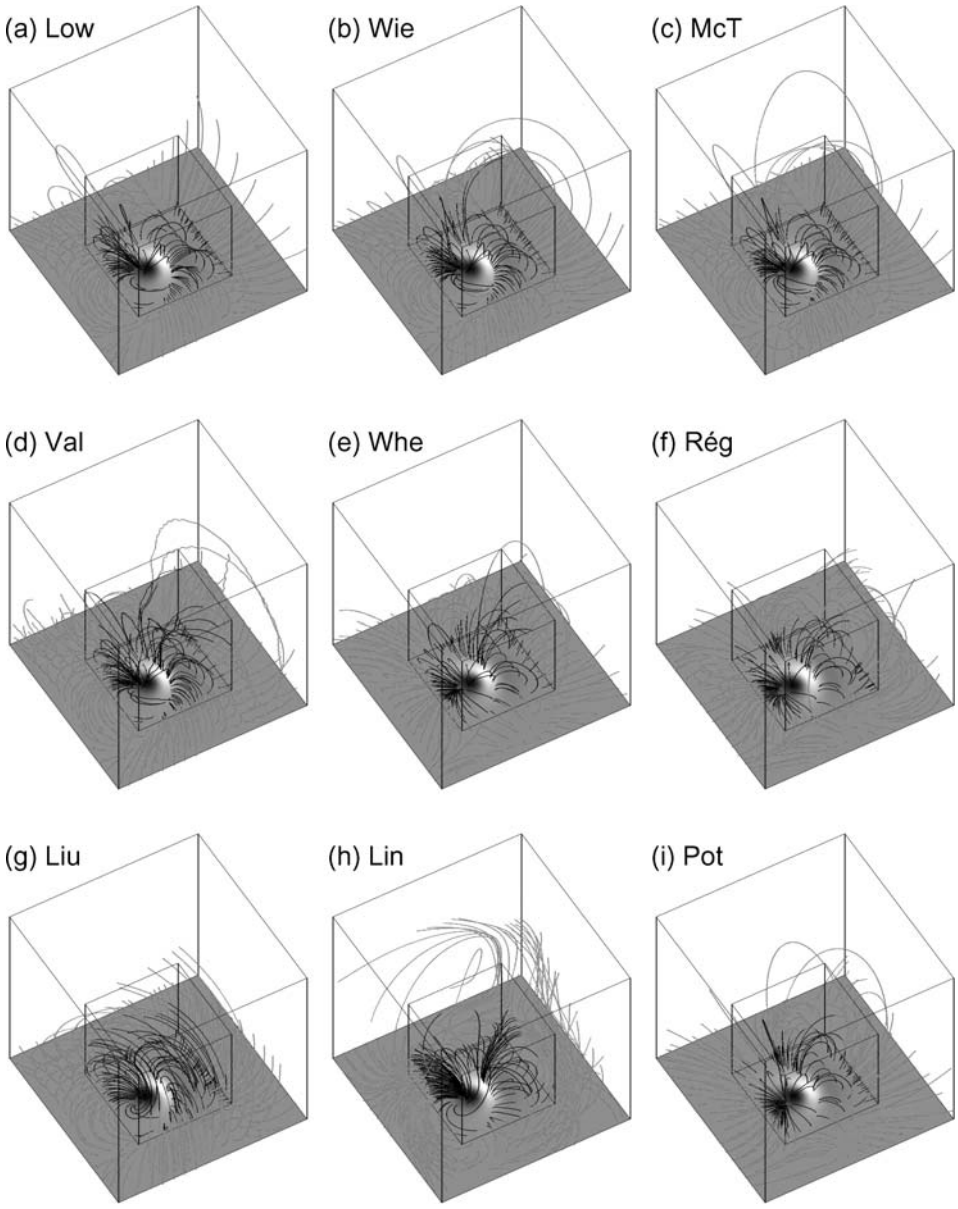

Figure 3. Same as Figure 1, but for analytical Case II, for which only the lower boundary was provided.

boundary is periodic in the Fourier solution of the linear force-free equations, but the magnetogram was padded with zeroes to reduce the effect of the periodicity. The constant value of the linear force-free parameter (α) was selected to minimize the differences between the horizontal field from the Low and Lou field and the

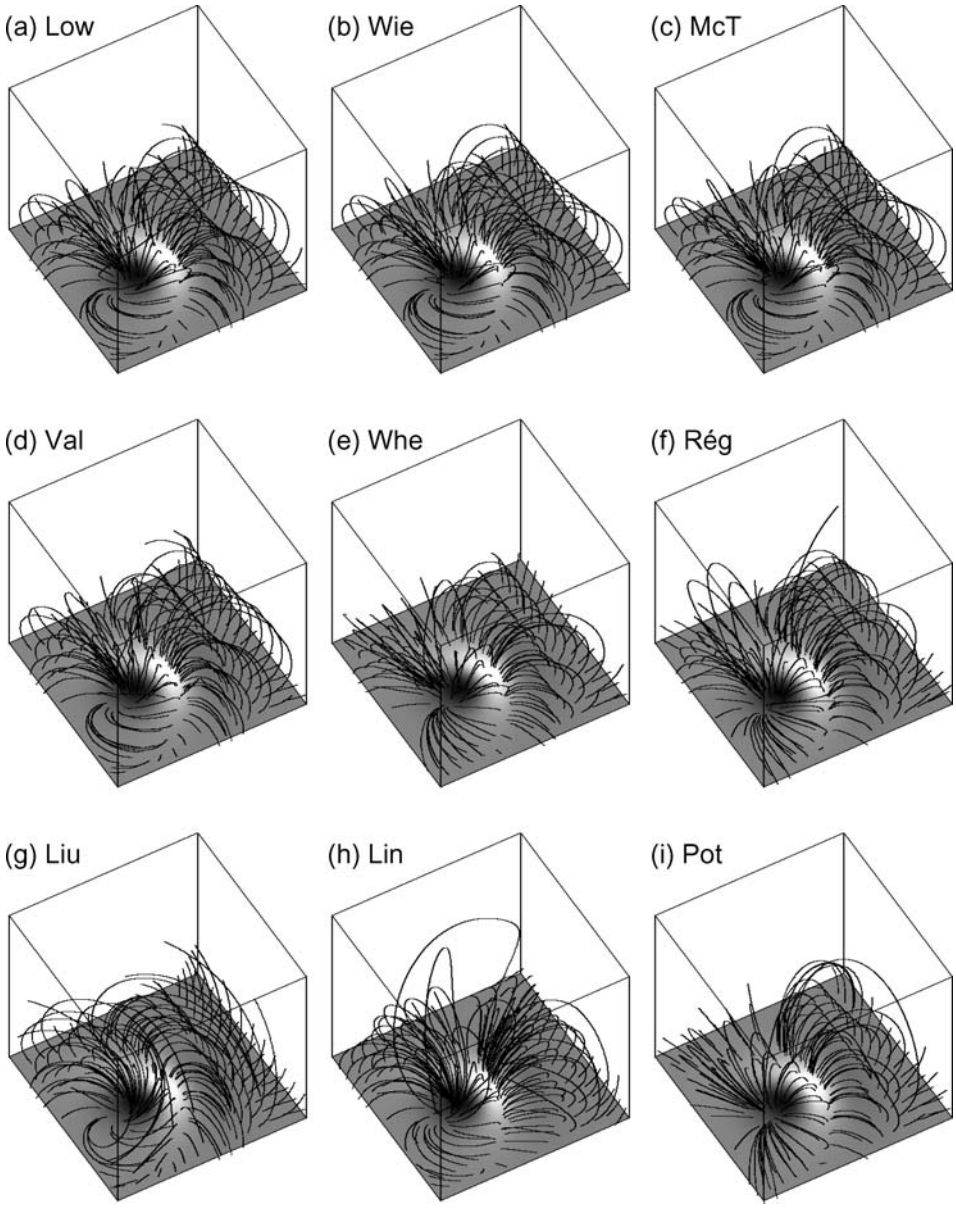

Figure 4. As Figure 3, but showing only the central domain of the model volume, as outlined by the small cube in Figure 3.

horizontal field from the linear force-free solution (the so-called α_{best} in, *e.g.*, Leka and Skumanich, 1999). The minimization was applied only over the core region of the Low and Lou solution. A potential field solution was also computed with this method by setting $\alpha \equiv 0$.

TABLE I

Model results for Case I, specifying all six sides of the box (upper table), and Case II, specifying only the lower boundary (bottom table).

Model	$C_{\rm vec}$[1]	$C_{\rm CS}$[2]	$E'_{\rm n}$[3]	$E'_{\rm m}$[4]	ϵ[5]	$\epsilon_{\rm P}$[6]	γ[7]	T[7]	BC[8]
(Case I) All boundaries provided, entire volume									
(a) Low and Lou	1	1	1	1	1	1.29	–		
(b) Wiegelmann	1.00	1.00	0.98	0.98	1.02	1.31	5		6**B**
(c) McTiernan	1.00	0.99	0.92	0.87	1.00	1.30	5		6**B**
(d) Valori	0.99	0.68	0.71	0.33	0.98	1.21	5		$\delta\mathbf{B}_\ell$
(e) Wheatland	0.98	0.83	0.64	0.42	0.90	1.17	6		$\delta\mathbf{B}_{\ell,+}$
(f) Régnier	0.93	0.49	0.41	0.09	0.80	1.04	6		$\boldsymbol{B}_{\ell,+}$, □
(g) Liu	0.88	0.46	−0.10	−3.00	1.13	1.47	6+		$\mathbf{B}_{\ell,+}$, ⊙
(h) LinearFF	0.88	0.90	0.50	0.42	0.77	1.00	∼3		$\alpha_{\rm best}$
(i) Potential	0.85	0.82	0.45	0.35	0.77	1	∼3		$B_{\ell,z}$
(Case II) Only lower boundary provided, entire volume									
(a) Low and Lou	1	1	1	1	1	1.10			
(b) Wiegelmann	1.00	0.57	0.86	−0.25	1.04	1.14		B	$\mathbf{B}_\ell$, Φ
(c) McTiernan	1.00	0.51	0.84	−0.38	1.04	1.14		C	$\mathbf{B}_\ell$, Φ
(d) Valori	0.99	0.55	0.75	−0.15	1.02	1.12		D	$\delta\mathbf{B}_\ell$
(e) Wheatland	0.99	0.58	0.69	0.13	0.96	1.05		E	$\delta\mathbf{B}_{\ell,+}$
(f) Régnier	0.94	0.28	0.49	−1.7	0.74	0.82		F	$\mathbf{B}_{\ell,+}$, □
(g) Liu	0.97	0.41	−0.02	−14.	1.00	1.09		G	$\mathbf{B}_{\ell,+}$, ⊙
(h) LinearFF	0.93	0.08	−0.80	−37.	1.04	1.15			$\alpha_{\rm best}$
(i) Potential	0.92	0.35	0.47	−0.63	0.91	1			$B_{\ell,z}$

Note. The letter coding in the first column is the same as for the panels in Figures 1–4. The NLFF field models are listed in order of decreasing quality of agreement, as ranked by the vector correlation, $C_{\rm vec}$, and the normalized vector error, or its listed complement $E'_{\rm n} = 1 - E_{\rm n}$. The linear force-free field and potential field cases are listed at the bottom of the tables.

[1] $C_{\rm vec}$, vector correlation, Equation (28).

[2] $C_{\rm CS}$, Cauchy-Schwarz, Equation (29).

[3] $E'_{\rm n} = 1 - E_{\rm n}$, complement of normalized vector error, Equation (30).

[4] $E'_{\rm m} = 1 - E_{\rm m}$, complement of mean vector error, Equation (31).

[5] ϵ, total magnetic energy normalized to the input case.

[6] $\epsilon_{\rm P}$, magnetic energy relative to a potential field.

[7] Scaling exponent for number of grid points, N, per dimension in the top panel, and computational resources and run times in the bottom panel: B = 15 minutes on two 666 MHz Compaq UNIX α processors ($80 \times 80 \times 72$ gridpoints); C = 14 hours on a 2.4 GHz processor ($102 \times 102 \times 101$ grid points); D = 2 hours on a four-processor Hitachi sr 8000; E = 9.5 hours on a dual 2.4 GHz Opteron; F = 56 hours on Sun V880 using 3 processors of 2 GB; G = 9 hours on 2.2 GHz Intel Pentium 4.

[8] 6**B**: vector field on all 6 sides; $\mathbf{B}_{\ell,+}$: vector field on (δ: partial) lower boundary in one polarity to derive α, using only the vertical field (B_z) in the other polarity; □: no field lines can leave the box; ⊙: no field assumed outside the box; $\alpha_{\rm fix}$: see Section 3.1; $B_{\ell,z}$: vertical component of photospheric field only; Φ: potential field specified on side and top boundaries.

TABLE II

As Table I, but for the inner volume of 32^3 pixels outlined by the cubes in Figures 1 and 3, showing only the figures of merit for Cases I and II in the top and bottom parts of the Table, respectively.

Model	C_{vec} [1]	C_{CS} [2]	E'_{n} [3]	E'_{m} [4]	ϵ [5]	ϵ_{P} [6]
(Case I) All boundaries provided, inner volume						
(a) Low and Lou	1	1	1	1	1	1.24
(b) Wiegelmann	1.00	1.00	0.97	0.96	1.02	1.26
(c) McTiernan	1.00	0.99	0.94	0.85	1.01	1.25
(d) Valori	1.00	0.98	0.90	0.87	0.98	1.21
(e) Wheatland	0.99	0.89	0.75	0.57	0.93	1.16
(f) Régnier	0.95	0.74	0.59	0.39	0.82	1.02
(g) Liu	0.98	0.85	0.71	0.43	0.89	1.11
(h) LinearFF	0.88	0.91	0.54	0.49	0.80	1.00
(i) Potential	0.86	0.87	0.50	0.44	0.81	1
(Case II) Only lower boundary provided, inner volume						
(a) Low and Lou	1	1	1	1	1	1.10
(b) Wiegelmann	1.00	0.91	0.92	0.66	1.04	1.14
(c) McTiernan	1.00	0.88	0.91	0.62	1.04	1.14
(d) Valori	0.99	0.82	0.83	0.39	1.02	1.12
(e) Wheatland	0.99	0.88	0.77	0.57	0.96	1.05
(f) Régnier	0.94	0.80	0.63	0.43	0.74	0.82
(g) Liu	0.97	0.54	0.48	−2.2	0.99	1.09
(h) LinearFF	0.94	0.53	0.39	−3.1	1.01	1.10
(i) Potential	0.92	0.66	0.57	0.30	0.91	1

3.2. NONLINEAR FORCE-FREE FIELDS

The six NLFF field modeling methods that are tested in this study fall into four general classes of algorithms:

1. *Optimization methods*, in which the field is evolved to match the boundary conditions, and the force-free and divergence-free conditions in some way that guarantees that the volume integral of the Lorentz force plus divergence (with weighted terms, if desired) always decrease;
2. *Magnetofrictional method*, in which the field is evolved by the Lorentz force acting against an artificial friction;
3. *Boundary integral methods*, in which the field is explicitly integrated for the boundaries and then iterated towards a best fit;
4. *Grad–Rubin like methods* in which a current-field iteration procedure is applied. A current distribution is chosen aligned with the initial field, the perturbation to

the field due to the currents is calculated, and then the current is redistributed along the perturbed field. This procedure is repeated until (hopefully) convergence is achieved. In some of these methods, the boundary currents are increased from step to step, gradually forcing the field away from an initial potential state.

We discuss examples of each type of method in order:

3.2.1. *Optimization methods*

Wheatland, Sturrock, and Roumeliotis (2000) developed a method that minimizes a joint measure (L) for the normalized Lorentz forces and the divergence of the field (each of which should equal zero, *c.f.*, Equations (1) and (2)) throughout the volume of interest, V:

$$L = \frac{1}{V}\int_V \left[B^{-2}\,|(\nabla\times\mathbf{B})\times\mathbf{B}|^2 + |\nabla\cdot\mathbf{B}|^2\right] \mathrm{d}V, \tag{6}$$

where $B = |\mathbf{B}|$.

This method involves minimizing the quantity L by optimizing the solution function $\mathbf{B}(\mathbf{x}, t)$ through states that are increasingly force- and divergence-free, where an artificial time-like parameter (t) is introduced as follows. Differentiating the expression for L by t yields integrals over the volume V and the bounding surface S:

$$\frac{1}{2}\frac{\mathrm{d}L}{\mathrm{d}t} = -\int_V \mathbf{F}\cdot\frac{\partial\mathbf{B}}{\partial t}\mathrm{d}V \; - \oint_S \mathbf{G}\cdot\frac{\partial\mathbf{B}}{\partial t}\mathrm{d}S, \tag{7}$$

where $\mathbf{G}$ – defined in Equation (8) in Wheatland, Sturrock, and Roumeliotis (2000) – can be ignored if $\frac{\partial\mathbf{B}}{\partial t} = 0$ on the boundary, and $\mathbf{F}$ is a function of the field ($\mathbf{B}$) with second-order derivatives:

$$\begin{aligned}\mathbf{F} = {} & \nabla\times(\boldsymbol{\Omega}\times\mathbf{B}) - \boldsymbol{\Omega}\times(\nabla\times\mathbf{B}) \\ & -\nabla(\boldsymbol{\Omega}\cdot\mathbf{B}) + \boldsymbol{\Omega}(\nabla\cdot\mathbf{B}) + (\boldsymbol{\Omega}\cdot\boldsymbol{\Omega})\mathbf{B},\end{aligned} \tag{8}$$

with the vector field $\boldsymbol{\Omega}$ defined by

$$\boldsymbol{\Omega} = B^{-2}\left[(\nabla\times\mathbf{B})\times\mathbf{B} - (\nabla\cdot\mathbf{B})\,\mathbf{B}\right]. \tag{9}$$

If the temporal evolution of $\mathbf{B}$ inside S is defined by $\partial\mathbf{B}/\partial t = \kappa\mathbf{F}$ (where $\kappa > 0$ is an arbitrary function, usually set to unity), setting $\partial\mathbf{B}/\partial t = 0$ on the boundary, then

$$\frac{\mathrm{d}L}{\mathrm{d}t} = -2\int_V \kappa F^2 \mathrm{d}V\ . \tag{10}$$

With this prescribed evolution, L is guaranteed to decrease in each step.

For each iteration step (k), the vector field $\mathbf{F}^{(k)}$ is calculated from the known field $\mathbf{B}^{(k)}$, then a new field may simply be computed as $\mathbf{B}^{(k+1)} = \mathbf{B}^{(k)} + \mathbf{F}^{(k)}\,\Delta t$ for small Δt, although a higher-order, smoother updating may also be employed.

3.2.1.1. Optimization Method, as Implemented by McTiernan. For Cases I and II in this paper, the starting point is a potential field extrapolated from the vector magnetogram, because the field is expected to be roughly potential far from active regions. The potential field extrapolation is derived from the Green's function solution of Chiu and Hilton (1977). For Case I, the initial field is potential inside the volume, but the Low and Lou vector field is used on the boundaries. For Case II, only the lower boundary magnetic vector field is used, while the initial field is taken to be potential elsewhere in the volume.

At the start of the iterative process, the field is thus only non-potential at the lower boundary. Non-potentiality propagates outward as the iterations increase.

The change in the objective function becomes smaller with each iteration. The code stops when $|\Delta L|/L$ reaches 10^{-8}, or ΔL becomes greater than zero.

For Case I, a uniform cubic grid is used with $N = 64$ grid points to each side. For Case II, a cube with $104^2 \times 102$ volume elements is used with a uniform spacing for the inner grid with $N = 64$, but with increased grid spacing beyond that in order to incorporate the field specified on a 192^2-pixel plane.

3.2.1.2. Optimization Method with Weighting Function; Wiegelmann. Wiegelmann (2004) introduces two weighting functions into Equation (6), thus expanding on the single-weighting-function approach suggested by Wheatland, Sturrock, and Roumeliotis (2000):

$$L_w = \frac{1}{V} \int_V \left[w_{\mathrm{f}}(\mathbf{r})\ B^{-2}\ |(\nabla \times \mathbf{B}) \times \mathbf{B}|^2 + w_{\mathrm{d}}(\mathbf{r})\ |\nabla \cdot \mathbf{B}|^2 \right] \mathrm{d}V, \tag{11}$$

where w_{f} and w_{d} are positive definite weighting functions for the force and divergence terms. For Case I, $w_{\mathrm{f}} = w_{\mathrm{d}} \equiv 1$. For Case II, for which only the bottom boundary data are given, Wiegelmann uses the position-dependent weighting functions to introduce a buffer boundary of $N_{\mathrm{b}} = 8$ grid points towards the side and top boundaries of the computational box. The weighting functions are chosen to be constant in the inner domain and drop to 0 with a cosine profile in the buffer boundary region.

The Wiegelmann algorithm starts with a potential field within the computational box, replaces either the bottom boundary or all six boundaries with the specified vector field as available, and proceeds to minimize the functional in Equation (11). The code checks if $L_w(t + \Delta t) < L_w(t)$ after each time step. If the condition is not fulfilled, the iteration step is repeated with Δt reduced by a factor of 2. After each successful iteration step, Wiegelmann's code increases Δt by a factor of 1.01 to allow the time step to become as large as possible with respect to the stability condition. The iteration stops if $|\frac{\Delta L_w}{\Delta t}|/L_w < 10^{-4}$ for 100 consecutive iterations.

The code has been applied to active regions by Wiegelmann *et al.* (2005a,b) and Wiegelmann, Inhester, and Sakurai (2005). The force-free optimization principle used here has been generalized to include non-magnetic forces like pressure gradients and gravity in Wiegelmann and Inhester (2003).

3.2.2. *Magnetofrictional Method, Valori*

The MHD relaxation method (Yang, Sturrock, and Antiochos, 1986; McClymont and Mikić, 1994; Roumeliotis, 1996; McClymont, Jiao, and Mikić, 1997) evolves a vector field into a nonlinear force-free field by integrating an approximate form of the MHD equations. As formulated by Roumeliotis (1996), the tangential components in the magnetogram plane are evolved from an initial (often potential) state to approach the vector magnetogram, which stresses the field at the bottom of the box (stress phase). In the subsequent relaxation phase, the system is driven toward a static state by integrating the MHD equations in an approximate form. A dissipative term, $\mathbf{D}(\mathbf{v})$, is included in the momentum equation,

$$\rho\left(\frac{\partial \mathbf{v}}{\partial t} + \mathbf{v}\cdot\nabla\mathbf{v}\right) + \nabla p = \mathbf{J}\times\mathbf{B} + \mathbf{D}, \tag{12}$$

where ρ is the plasma density, $\mathbf{v}$ the velocity, and p the gas pressure. This dissipative term must vanish for vanishing velocities, but can otherwise be specified relatively arbitrarily, since intermediate states of the field in the course of the stress-and-relax procedure are considered to possess no physical significance. A series of stress-and-relax cycles can be applied until the tangential components of the magnetogram are matched to some specified degree. If an equilibrium is reached, then any non-zero terms in Equation (12) correspond to real Lorentz forces and pressure-gradient forces. If the additional assumption of low plasma β is made, as is done here, then the pressure term drops out so that a fully relaxed field satisfies the force-free condition of Equation (1).

Here, the specific version of the so-called magneto-frictional method (Yang, Sturrock, and Antiochos, 1986) is adopted, which for plasma $\beta = 0$ neglects the entire left-hand side of Equation (12) and uses a friction-like dissipative term: $\mathbf{D}(\mathbf{v}) = -\nu\,\mathbf{v}$. Hence, Equation (12) reduces to

$$\mathbf{v} = \frac{1}{\nu}\mathbf{J}\times\mathbf{B}, \tag{13}$$

leaving only the induction equation

$$\frac{\partial \mathbf{B}}{\partial t} = \nabla\times(\,\mathbf{v}\times\mathbf{B}\,), \tag{14}$$

with $\mathbf{v}$ specified by Equation (13). The quantity ν is chosen here to be a convenient function of space, that optimizes the progress of the relaxation throughout the box (Yang, Sturrock, and Antiochos, 1986), and it is also chosen to be time dependent to reduce oscillations in the final phase of the relaxation (Valori, Kliem, and Keppens, 2005).

On the photospheric boundary the general stress-and-relax strategy prescribes how to impose the magnetic field. Results of a single-step stress version of the method are presented here, *i.e.*, the magnetogram is directly overwritten onto the photospheric boundary before the system is advanced in time. At the side and top boundaries, the tangential components of the magnetic field are linearly

extrapolated onto ghost cell layers, while the normal component is fixed at each iteration by requiring that the field remains divergence free. Additionally, a boundary layer (of three and seven points in Cases I and II, respectively) is used where the velocity field (Equation (13)) is windowed in the outer part of the grid by a parabolic decrease toward all of the boundaries except $z = 0$.

Finally, the divergence-free property of the relaxed magnetic field is ensured by a diffusive approach (Marder, 1987; Dedner *et al.*, 2002).

At the present stage of code development, the spatial discretization is a pure second-order central differencing combined with a time stepping in a single-step forward Eulerian manner, where the time stepping is dynamically adapted in order to insure stability. Such simple discretization leads to an even-odd grid point decoupling that results in a weak spatially oscillating modulation of the field values (Valori, Kliem, and Keppens, 2005). This aspect of the implementation and speed optimization are currently being improved.

In both Cases I and II, only information from the photospheric boundary was used. The results presented here were obtained on grids of $66 \times 66 \times 70$ for Case I and $86 \times 86 \times 80$ for Case II.

3.2.3. *Iterative Boundary Integral Method; as Used by Liu*

Yan and Sakurai (1997, 2000) proposed an integral equation representation for a nonlinear force-free field in terms of the field and its normal gradient at the boundary. In their model, the field ($\mathbf{B}_0$) at the lower boundary surface (S_0) can be taken from observations or models. The upper boundary is open to infinity, and field is assumed to vanish following an asymptotic condition, $\mathbf{B} = O(\frac{1}{r^2})$ for $r \to \infty$ which ensures a finite energy content.

Yan and Sakurai (2000) showed how Green's second identity allows the solution of the force-free field with these boundary conditions to be represented by a surface integral involving the values and gradients normal to the surface of the magnetic field $\mathbf{B}$ and an auxiliary function $\bar{\mathbf{Y}}$:

$$c_i \mathbf{B}_i = \oint_S \left(\bar{\mathbf{Y}} \frac{\partial \mathbf{B}}{\partial n} - \frac{\partial \bar{\mathbf{Y}}}{\partial n} \mathbf{B} \right) \mathrm{d}S, \tag{15}$$

where $c_i = 1$ for point i in the volume V and $c_i = 1/2$ if i is on the volume's surface (S). The auxiliary function $\bar{\mathbf{Y}}$ is written as a diagonal matrix,

$$\bar{\mathbf{Y}} = \mathrm{diag}\{Y_x, Y_y, Y_z\} = \mathrm{diag} \left\{ \frac{\cos(\lambda_x r)}{4\pi r}, \frac{\cos(\lambda_y r)}{4\pi r}, \frac{\cos(\lambda_z r)}{4\pi r} \right\}. \tag{16}$$

where r is the distance between point i and another point for which $\bar{\mathbf{Y}}$ is computed. The vector field specified by the three components λ_p ($p = x, y, z$) is determined by the requirement that the field vanishes at infinity, which is true if

$$\int_V Y_p \left[\lambda_p^2 B_p - \alpha^2 B_p - (\nabla \alpha \times \mathbf{B})_p \right] \mathrm{d}V = 0, \quad p = x, y, z \tag{17}$$

Yan and Sakurai (2000), note that Equation (17) does not necessary hold for the near field, but the method as implemented prescribes it.

This model can be numerically solved by an iterative process. If one assumes at internal points $\mathbf{B}^{(-1)} = 0$ and at the boundary that the gradient normal to the surface S is zero, *i.e.*, that $\partial \mathbf{B}^{(-1)}/\partial n = 0$, and one starts from $k = 0$, the force-free field represented by the boundary integral equation can be calculated. For each boundary node point with $\lambda_x^{(k)}$, $\lambda_y^{(k)}$, $\lambda_z^{(k)}$ one has in this first step from Equation (15) that

$$\frac{1}{2}\mathbf{B}_{0i} = \oint_S \left(\bar{\mathbf{Y}}^{(k)} \frac{\partial \mathbf{B}^{(k)}}{\partial n} - \frac{\partial \bar{\mathbf{Y}}^{(k)}}{\partial n} \mathbf{B}_0 \right) \mathrm{d}S. \tag{18}$$

The boundary unknowns $\partial \mathbf{B}^{(k)}/\partial n$ can be obtained from Equation (18) by the boundary element method for arbitrary boundary shape with prescribed boundary values $\mathbf{B}_0$. Then for each internal point in V with $\lambda_x^{(k)}$, $\lambda_y^{(k)}$, $\lambda_z^{(k)}$, the field $\mathbf{B}_i^{(k)}$ can be computed by

$$\mathbf{B}_i^{(k)} = \oint_S \left(\bar{\mathbf{Y}}^{(k)} \frac{\partial \mathbf{B}^{(k)}}{\partial n} - \frac{\partial \bar{\mathbf{Y}}^{(k)}}{\partial n} \mathbf{B}_0 \right) \mathrm{d}S, \tag{19}$$

The iteration stops when $|\mathbf{B}^{(k)} - \mathbf{B}^{(k-1)}| < \delta$, where δ is a small positive number. As long as this is not satisfied, the process iterates by modifying λ_x, λ_y, λ_z to reach a nonlinear force-free solution. The scheme to iterate the functions λ_p is described by Yan and Sakurai (2000) in their Section 4.1.

The process must also maintain $|\partial \mathbf{B}^{(k)}/\partial n - \partial \mathbf{B}^{(k-1)}/\partial n| < \delta_S$ on the boundary, where δ_S is a small positive number. If this inequality is not satisfied, then Equation (18) is iterated until it is. Once the inequality is met, then set $\partial \mathbf{B}^{(k+1)}/\partial n = \partial \mathbf{B}^{(k)}/\partial n$ and go to Equation (19) for the next iteration.

The input to this model is the known field over an arbitrarily-shaped local boundary as stated in Yan and Sakurai (2000), and it is assumed that the flux extends from the surface in all directions to infinity from the boundary surface so that the net flux is zero in the volume. That allows the side boundary conditions to be incorporated in the model by applying the equivalence principle as described in Yan and Liu (1995). However, in the above iterative process, the volume integration is only carried out over an appropriately large space, which introduces a truncation error in the numerical results.

The numerical code of this method has been used to model soft X-ray loops seen in *Yohkoh* images (Wang *et al.*, 2000; Liu *et al.*, 2002) and to model a magnetic flux rope (Yan *et al.*, 2001). These tasks, however, did not carry out an iteration to search for λ. An attempt was made to verify the existence of λ factors by Li, Yan, and Song (2004).

For Case I, the three components of magnetic field (B_x, B_y, B_z) on the lower boundary and the four side boundaries were used. For Case II, the vector field over the whole lower boundary (192×192) was employed. For both cases, no iteration was performed to determine the set of λ factors, because at our resolution the code required 80 hours for the first step only, deemed too long to be practical. However,

a new algorithm has been developed recently, and has been proven to be feasible and effective (Yan and Li, 2005). It greatly reduces the computation time, so that completion of the iteration appears feasible in the near future.

3.2.4. *Iterative Grad–Rubin-Like Methods*

3.2.4.1. Grad–Rubin-like as implemented by Régnier. Régnier adopted the approach proposed by Grad and Rubin (1958) and implemented by Amari and colleagues to solve the nonlinear force-free reconstruction problem as a well-posed boundary value problem (Amari *et al.*, 1997; Amari, Boulmazaoud, and Mikić, 1999). He computes the nonlinear force-free magnetic field in a volume by solving two sets of equations iteratively for each step k:

$$\mathbf{B}^{(k)} \cdot \boldsymbol{\nabla}\alpha^{(k)} = 0 \quad \text{in } V \tag{20}$$

$$\alpha^{(k)}|_{S^{\pm}} = h \tag{21}$$

and

$$\boldsymbol{\nabla} \times \mathbf{B}^{(k+1)} = \alpha^{(k)}\mathbf{B}^{(k)} \quad \text{in } V \tag{22}$$

$$\boldsymbol{\nabla} \cdot \mathbf{B}^{(k+1)} = 0 \quad \text{in } V \tag{23}$$

$$B_z^{(k+1)}|_{S^{\pm}} = g \tag{24}$$

$$\lim_{|r|\to\infty} |\mathbf{B}^{(k+1)}| = 0 \tag{25}$$

where S is the surface of the volume V and $S^{\pm}$ corresponds to the surface where the normal component of $\mathbf{B}$ is positive or negative. To ensure that the divergence of $\mathbf{B}$ vanishes, the two sets of equations are reformulated using the vector potential $\mathbf{A}$ associated with $\mathbf{B} = \nabla \times \mathbf{A}$ (see Amari, Boulmazaoud, and Mikić, 1999).

To compute the NLFF field, a staggered grid is used in order to define the magnetic field, the vector potential, and their derivatives. For the test cases, we use a uniform grid similar to the analytical input cases. the effect of the staggered uniform grid results in some discrepancies at the bottom boundary as shown by Amari, Boulmezaoud, and Aly (2005).

The bottom boundary conditions g and h are the vertical magnetic field on the entire surface and the torsion function α specified for one polarity. Regions for which B_z and $B_\perp$ are below a certain threshold are assumed to be potential; this affects 1.4% of the area for Case I and 3.2% of the area in the 64^2-pixel model region for Case II. On the other boundaries, Equation (25) is satisfied by imposing that no field line leaves the volume, *i.e.*, that $\mathbf{B} \cdot \mathbf{n} = 0$ (for $\mathbf{n}$ normal to S) at the boundary, and that $\alpha \equiv 0$ there.

The iterative scheme is initiated from a potential field with the vertical magnetic field component as bottom boundary conditions and satisfying $\mathbf{B} \cdot \mathbf{n} = 0$ on the other boundaries. The algorithm then starts with the α distribution multiplied by

a small constant by solving Equations (20) and (21), and a new magnetic field configuration is then computed by solving Equations (22)–(25). The algorithm then increases the multiplier for the bottom α field, and iterates until the full value of α is reached.

The numerical code has been successfully tested on Low and Lou (1990) solutions, and has been applied to solar active regions by, *e.g.*, Régnier, Amari, and Kersalé (2002), Bleybel *et al.* (2002), Régnier and Amari (2004), and Régnier and Canfield (in preparation).

3.2.4.2. Grad–Rubin-like, as Implemented by Wheatland. Wheatland (2004) presented a new approach to calculating force-free fields which is similar to that of Sakurai (1981). In Sakurai's approach, the current distribution is modeled in terms of cylindrical current elements between nodal points on a small number of field lines originating from a chosen polarity of field, and then the Lorentz force is calculated at each nodal point due to all current elements using an exact integral solution to Ampère's law. The free parameters in the problem were taken to be the positions of the nodal points. Requiring the Lorentz force to vanish at all nodal points gave a set of simultaneous nonlinear equations for the nodal point positions, which were solved. Wheatland (2004) models the current in the same way, but calculates the field due to the currents directly at all gridpoints at each iteration rather than only at the nodal points. Adding this field to the initial potential field gives an updated field. The field lines of this field are traced and form the basis for the current distribution for the next iteration. The method is straightforward to parallelize, with the field contributions from different current-carrying field lines being divided up among the processes. Versions of the code for distributed memory computers (using the Message Passing Interface, MPI) and for shared memory computers (using OpenMP) have been written.

The code used by Wheatland (2004) contained an error in the representation of the current; the current density was too large in regions of weak field. Correction of this error, as was done in the code used in this study, leads to greatly improved results. It is possible to calculate fields with much larger boundary values of α than shown in that study, and the calculated fields are considerably closer to being force-free.

The boundary conditions on current in the Wheatland (2004) method are the values α_i of the force-free parameter over one polarity of the field. The method is straightforward to apply to cases with highly localized currents, *i.e.*, when only a small number of boundary points have non-zero α_i. However, for our two Low and Lou (1990) test cases, the currents are widely distributed on the lower boundary. This causes two problems. First, the set of $\approx \frac{1}{2}N^2$ grid points in the lower boundary with a chosen polarity is too large for a practical calculation. Second, if currents are widely distributed, many gridpoints with non-zero α_i will have field lines which close outside the boundary region, and the method is not expected to work for these field lines. A practical approach to these problems is first to set α_i to zero at

all but a relatively small fraction of boundary points. Only points $(x_i, y_i, 0)$ with both

$$B_z(x_i, y_i, 0) > f_{\mathrm{B}} \times \max[B_z(x_i, y_i, 0)] \tag{26}$$

and

$$J_z(x_i, y_i, 0) > f_{\mathrm{J}} \times \max[J_z(x_i, y_i, 0)] \tag{27}$$

are chosen to have non-zero $\alpha_i = \mu_0 J_z / B_z$, where f_{B} and f_{J} are constants (set to 0.005 in Case I and 0.001 in Case II). Second, field lines which leave the box have α_i set to zero on them, even if they satisfy the above conditions. These conditions mean that the fields calculated with the method have different boundary conditions from the exact Low and Lou (1990) solutions. The values of f_{B} and f_{J} are set so that the total number of points for which $\alpha_i \neq 0$ is kept relatively small, set at 5% for cases I and II in this study.

3.3. Order of the Methods

It is interesting to consider the orders of the methods (*cf*, Table I). The optimization method scales with the number (N) of resolution elements for each side of the model volume as N^5 (Wheatland, Sturrock, and Roumeliotis, 2000); that same scaling holds for the magnetofrictional method. The Grad–Rubin-like methods scale as N^6 (see, *e.g.*, Wheatland, 2004). The boundary element method of Yan and Sakurai (2000) involves the evaluation of a volume integral for each point, and hence is at least of order N^6; if the required number of iterations also scales with N, the order is higher.

4. Figures of Merit

In order to quantify the degree of agreement between vector fields $\boldsymbol{B}$ (for the input model field) and $\boldsymbol{b}$ (the NLFF model solutions) that are specified on identical sets of grid points, we use five metrics that compare either local characteristics (*e.g.*, vector magnitudes and directions at each point) or the global energy content in addition to the force and divergence integrals.

The vector correlation (C_{vec}) metric is analogous to the standard correlation coefficient for scalar functions:

$$C_{\mathrm{vec}} \equiv \sum_i \boldsymbol{B}_i \cdot \boldsymbol{b}_i \Bigg/ \left(\sum_i |\boldsymbol{B}_i|^2 \sum_i |\boldsymbol{b}_i|^2 \right)^{1/2}, \tag{28}$$

where $\boldsymbol{B}_i$ and $\boldsymbol{b}_i$ are the vectors at each point i. If the vector fields are identical, then $C_{\mathrm{vec}} \equiv 1$; if $\boldsymbol{B}_i \perp \boldsymbol{b}_i$, then $C_{\mathrm{vec}} \equiv 0$.

The second metric, $C_{\rm CS}$ is based on the Cauchy-Schwarz inequality ($|\boldsymbol{a}\cdot\boldsymbol{b}| \leq |\boldsymbol{a}||\boldsymbol{b}|$ for any two vectors $\boldsymbol{a}$ and $\boldsymbol{b}$):

$$C_{\rm CS} \equiv \frac{1}{M}\sum_i \frac{\boldsymbol{B}_i\cdot\boldsymbol{b}_i}{|\boldsymbol{B}_i||\boldsymbol{b}_i|} \equiv \frac{1}{M}\sum_i \cos\theta_i, \tag{29}$$

where M is the total number of vectors in the volume, and θ_i the angle between input and model magnetic fields at point i. This metric is mostly a measure of the angular differences of the vector fields: $C_{\rm CS} = 1$ when $\boldsymbol{B}$ and $\boldsymbol{b}$ are parallel and $C_{\rm CS} = -1$ if they are anti-parallel; $C_{\rm CS} = 0$ if $\boldsymbol{B}_i \perp \boldsymbol{b}_i$ at each point.

Next, we introduce two measures for the vector errors, one normalized to the average vector norm, one averaging over relative differences. The normalized vector error $E_{\rm n}$ is defined as

$$E_{\rm n} = \sum_i |\boldsymbol{b}_i - \boldsymbol{B}_i| \Big/ \sum_i |\boldsymbol{B}_i|. \tag{30}$$

The mean vector error $E_{\rm m}$ is defined as

$$E_{\rm m} = \frac{1}{M}\sum_i \frac{|\boldsymbol{b}_i - \boldsymbol{B}_i|}{|\boldsymbol{B}_i|}. \tag{31}$$

Unlike the first two metrics, perfect agreement of the two vector fields results in $E_{\rm m} = E_{\rm n} = 0$. For an easier comparison with the other metrics, we list $E'_{\rm m,n} \equiv 1 - E_{\rm m,n}$ in Tables I and II so that all measures in these tables reach unity for a perfect match.

As we are also interested in determining how well the models estimate the energy contained in the field, we use the total magnetic energy in the model field normalized to the total magnetic energy in the input field as a global measure of the quality of the fit:

$$\epsilon = \frac{\sum_i |\boldsymbol{b}_i|^2}{\sum_i |\boldsymbol{B}_i|^2}. \tag{32}$$

For comparison, Tables I and II also list $\epsilon_{\rm P}$, defined as the total magnetic energy normalized to the total magnetic energy in the corresponding potential-field solution.

The degree of convergence towards a force-free and divergence-free model solution can be quantified by the integral measures of the Lorentz force and divergence terms in the minimization functional in Equation (6), computed over the entire model volume V, normalized to a unit volume (pixel) to allow comparison at different resolutions:

$$\begin{aligned} L_{\rm f} &= \frac{1}{V}\int_V B^{-2}\,|(\nabla\times\mathbf{B})\times\mathbf{B}|^2\,{\rm d}V \\ L_{\rm d} &= \frac{1}{V}\int_V |\nabla\cdot\mathbf{B}|^2\,{\rm d}V \\ L &= L_{\rm f} + L_{\rm d} \end{aligned} \tag{33}$$

TABLE III

Experimenting with weights and boundaries with the Wiegelmann code for the Wheatland optimization method.

w_f	w_d	N_b	Start	L	L_f	L_d	$\sigma_J \times 10^2$
Varying buffer depths							
1	1	0	Potential	0.19	0.12	0.069	7.0
1	1	8	Potential	0.18	0.11	0.066	5.7
1	1	16	Potential	0.18	0.11	0.065	5.5
1	1	32	Potential	0.18	0.11	0.065	5.5
Varying initial conditions							
1	1	8	LFF $\alpha_L = +3$	0.20	0.12	0.08	7.0
1	1	8	LFF $\alpha_L = -3$	0.21	0.13	0.08	7.3
1	1	8	Vertical	0.91	0.62	0.30	16.0
1	1	8	Random	33.0	24.0	9.3	33.0
Varying weights							
0	1	8	Potential	55.0	55.0	3.3×10^{-6}	57.0
1	0	8	Potential	7.5	0.019	7.5	3.7
0.1	1	8	Potential	7.4	7.0	0.4	24.0
1	0.1	8	Potential	0.44	0.039	0.4	6.0

Note. The first four columns specify boundary parameters and initial conditions: w_f and w_d are the weighting function of the force-free and divergence-free conditions, respectively; N_b is the number of grid points in the buffer boundary layer; the fourth column specifies the initial field in the volume (including the lateral and top boundaries of the computational box). The final four columns show the measures L, L_f, L_d, and σ_J defined in Equations (33) and (34).

where L_f and L_d measure how well the force-free and divergence-free conditions are fulfilled, respectively. Another possible measure of how well the force-free condition is met is the current-weighted average of the sine of the angle between the magnetic field and the electrical current density (see Wheatland, Sturrock, and Roumeliotis, 2000, for details.)

$$\sigma_J = \left(\sum_i \frac{|\mathbf{J}_i \times \mathbf{B}_i|}{B_i} \right) / \sum_i J_i . \tag{34}$$

These measures are used in Table III and discussed in Section 5.3.

5. Analytical Test Cases

5.1. Case I: All boundary conditions provided

Figure 1 compares the input model and results for Case I for which the vector field on all six side boundaries was provided to the modelers. A visual inspection of

the field-line patterns seen from above resulted in the following order: best were the Wiegelmann and McTiernan solutions, then, in order, the Valori, LFF field, Wheatland, potential, Régnier, and Liu solutions. Figure 1 shows these in order for the NLFF field cases, followed by the LFF and potential cases for comparison in the bottom row.

A visual inspection is, of course, strongly influenced by the appearance of field lines in the (large) weak-field region. Nevertheless, the ordering of the results by the quality of visual agreement corresponds remarkably well with the numerical ordering of the figures of merit for the vector comparisons defined in Equations (28)–(31) shown in Table I. Both of the vector-error metrics $E'_{\mathrm{m,n}}$ are based on a mean of the difference between the field vectors relative to the input field vectors. These measures thus include information on both the agreement in direction and magnitude. The other two vector correlations, C_{vec} and C_{CS}, are relatively more strongly influenced by the directional differences between the vectors. We continue the discussion of the figures of merit in Section 5.2, except to point out that the ordering of the results is very nearly the same if the figures of merit are computed for a 32^3-pixel volume over the center of the surface field (Table II, Figure 2). Note that all figures of merit are better for this core volume, mainly because this volume is further away from the boundaries and because the lower boundary is included more completely in the strong-field, strong-current interior in the methods of Wheatland and Régnier.

The best-fit model results by Wiegelmann and McTiernan closely correspond to the input model, both in the appearance of the field line configurations and in matching the vector fields: the figures of merit show that the average angular differences between the input and modeled fields differ by less than a few degrees and the relative vector norms differ by only 2% for the Wiegelmann case to 13% for the McTiernan solution. We thus confirm that there are successful methods to recover a NLFF field (or at least our test fields) in cases where all boundary conditions are entirely specified.

The magnetofrictional "stress and relax" model by Valori ranks third, performing only somewhat worse than the Wiegelmann and McTiernan models for the inner half of the volume in Case I, despite the fact that only the lower boundary vector field was used as boundary information. The Valori and Wheatland models perform comparably with different rankings for the different metrics for the full volume.

The fourth-ranking solution is the Grad–Rubin-like code implemented by Wheatland. In this model, only part of the vector field on the lower boundary is used to specify an α map for one polarity. Specifically, the α map covers fewer than 5% of the pixels in the Low–Lou solution, which includes 97% of the total unsigned current density in the lower boundary. The Wheatland solution still recovers some of the overall geometry of the field (as does even the potential field), but it yields an energy estimate that measures only approximately half of the energy increment relative to the potential case, *i.e.*, $(\epsilon_{\mathrm{Wheatland}} - \epsilon_{\alpha=0})/(\epsilon_{\mathrm{Low-Lou}} - \epsilon_{\alpha=0}) = 0.59$. The reason is that so many current-carrying field lines in the Low–Lou field leave the box, for which α is set to zero in the Wheatland code.

The Régnier model is next down the list. Note that its boundary condition on the five side and top boundaries allows no field lines to escape (equivalent to having perfectly conducting side boundaries) and that all field lines that touch the side and top boundaries carry no current. These boundaries lie 32 pixels outside the volume of the 64^3 cube shown in Figure 1, however, so the field lines apparently leaving the volume shown in the figure in fact swirl around to return elsewhere on the boundaries of the volume shown.

In Case I, the problem encountered by the Régnier algorithm appears to be that too much of the α field, and even of the flux involved, lies outside the modeled volume, combined with the fact that the model's application imposes a lower limit to $|\alpha|$, below which it sets $\alpha \equiv 0$ in order to deal with what would be noisy data for real observations (although that involves only a small fraction of the area for our Cases I and II). These field lines, now potential, cannot leave the box, so must swirl around the volume to connect to other potential field lines. Note that the Wiegelmann and McTiernan solutions do not suffer from this problem, because their method allows full implementation of the vector boundary field or, in McTiernan's case, at least of the potential approximation of that field, which allows the field outside the box to communicate most of its presence to the field to be modeled.

The worst match is found for the Liu model. One important cause for this is that the model was allowed to make only a single step in its iteration cycle. On completing that first step, the code had already used over 80 hours of CPU time, which was deemed far too long for a useful code for practical applications when considering that many steps would have to be taken to reach any convergence. This leaves the question whether the algorithm would in principle have converged for the test cases unanswered, but initial low-resolution tests by Yan and Sakurai (2000) suggest that convergence is possible in principle; moreover, Yan and Li (2005) have developed a new code recently to considerably reduce the computation time.

5.2. Case II: Lower boundary over an extended area

For Case II only the lower boundary is specified, but with an apron around the base that is as wide as the central volume of interest, *i.e.*, the lower vector field boundary is provided for a 192×192 pixel area for which only the central 64×64 region is to be modeled. For this case, we chose a length scale for the Low–Lou solution that places most of the flux within the central region, with all but a very small fraction of field and currents contained in the apron area around the 64×64 model region.

The results are shown in Figures 3 and 4 (with panels in the same order as in Tables I and II and Figures 1 and 2). A visual inspection of the field line patterns seen from above, as we did for Case I, resulted in the same order of goodness of fit as for Case I for the NLFF field models. This is not surprising because for all but the Wiegelmann and McTiernan models, the boundary condition information was in fact applied in the same manner by the codes. For the Wiegelmann and

McTiernan models, the five side and top boundaries were specified as computed from the potential field solution based on the extended area for which the lower boundary was specified

It is interesting to note that all models match the inner part of the field configuration significantly better than the more distant field (compare Figures 1 and 3 to Figures 2 and 4, and Table I to II). In the inner volume, the vector magnetic field and the scalar $|\alpha|$ field are both relatively large, while α is more comprehensively used by the Grad–Rubin-like methods as implemented by Régnier and by Wheatland.

The figures of merit for Case II for the Wiegelmann and McTiernan solutions, as listed in the lower parts of Tables I and II, show an essentially perfect vector correlation $C_{\rm vec}$, a normalized vector error suggesting an average relative deviation of 10 – 15%, and an energy estimate that is close to the actual value (in fact exceeding the Low–Lou value by 2%). The values of $C_{\rm CS}$ and $E'_{\rm m}$, in contrast, deviate quite strongly from the optimal value of unity. This is caused by relatively strong deviations high in the simulated volume, where the field is weak, and where the field geometry is not probed by the field lines in Figure 3 which all stay rather low in the box owing to the strong field gradient with height.

5.3. Effects of a tapered boundary and initial conditions

Having established that the Wiegelmann and McTiernan codes perform best, we now focus on the faster of these two, the Wiegelmann code, to investigate in some more detail the dependence of the results on the application of the boundary conditions for Case I and on the choice of initial conditions.

As a first test of the effects of the side and top boundary conditions, we investigate how the depth $N_{\rm b}$ of a buffer boundary influences the quality of the reconstruction as measured by $L_{f,d}$ in Equation (33). Rows 1 – 4 in Table III show that the value of $N_{\rm b}$ has only a small influence on the result, primarily because the magnetic flux for this test case is concentrated well into the interior of the box. Wiegelmann (2004), in contrast, found that larger boundary layers provide better results for a case with more magnetic flux close to the boundaries of the model volume.

Rows 5 – 8 in Table III show the effects of different initial conditions, including the lateral and top boundary conditions. As initial conditions we used (1) a potential field computed with the Green's function method (Aly, 1989), (2) linear force-free fields with either positive or negative α as computed with the method of Seehafer (1978), (3) a strictly vertical field based on B_z at the bottom boundary, and (4) random numbers for all three field components of the field throughout the box.

We find that an initial potential field provided the best result, being slightly better than the case starting with a linear force-free field (for which a positive value of α was slightly better than a negative one). The rather un-physical initial vertical field gave significantly worse results, and random numbers as initial state gave by far the worst result. Clearly, starting from a state near that of the true field is beneficial for a

rapid convergence, and in some cases necessary to allow the algorithm to converge at all.

Rows 2 and 9 – 12 of Table III show the effects of different weights for the force (w_f) and divergence (w_d) terms. If we minimize only for a divergence-free condition and ignore the force-free condition (line 9 of the table), we find – as expected – a very low value of the divergence measure L_d, but high values for the force measure L_f and the angle between forces and currents as characterized by σ_J. Ignoring the divergence-free condition completely results naturally in the opposite result. The sum value L of the force and divergence measures is for both cases much higher than for the case with $w_f = w_d = 1$. This is also true if we weight the force and divergence measures by relative weights that differ by an order of magnitude. We conclude, therefore, that the optimal choice is to use equal weights $w_f = w_d$ for force and divergence terms in the minimization functional in Equation (11).

6. Electrical Currents and Field Energy

Figures 5 and 6 compare the input model vector field and electrical currents, respectively, with the Wiegelmann model for Case II (showing only the inner 32^2-pixel area). Panels *b* show that the vector magnetic field is matched very well at the base (as the lower-boundary condition should if implemented optimally), although there are relatively strong differences over the central region in the horizontal current. The good agreement of the analytical and model vector magnetic fields reflects that the boundary magnetic field was – as expected – properly held fixed in the numerical code. The vertical electrical current density at the lower boundary follows directly from the derivatives of $B_{x,y}(z = 0)$ and are approximated well by the second-order differencing scheme used. Computation of the horizontal electrical current density, in contrast, requires information from the model field immediately above the lower boundary; the one-sided second-order differencing scheme then reflects any deviations in the modeled field even on the lower boundary. These differences reach up to just over 10% of $\mathbf{J} \times \mathbf{n}$ in the Wiegelmann solution shown.

The higher field (up to 25% of the volume height in panel *d*) is matched relatively well, while the electrical currents show a pattern suggestive of a slight distortion of the overall volume (magnetic and current) field. The currents related to these distortions in fact raise the estimate of the total energy content of the central volume over the model's energy content by a few percent, or by almost 30% relative to the energy in the potential field model, both for the inner 32^3-pixel volume and for the entire 64^3-pixel volume. This similarity in behavior is not unexpected, because most of the field energy is concentrated near the sources. For Case I this difference was less than 8%. As the field in Case I was less compact than in Case II, we suggest that the larger deviation in energy estimate for Case II is not so much the consequence of the difference in boundary conditions, but rather that there is more structure in the field than the models can handle well.

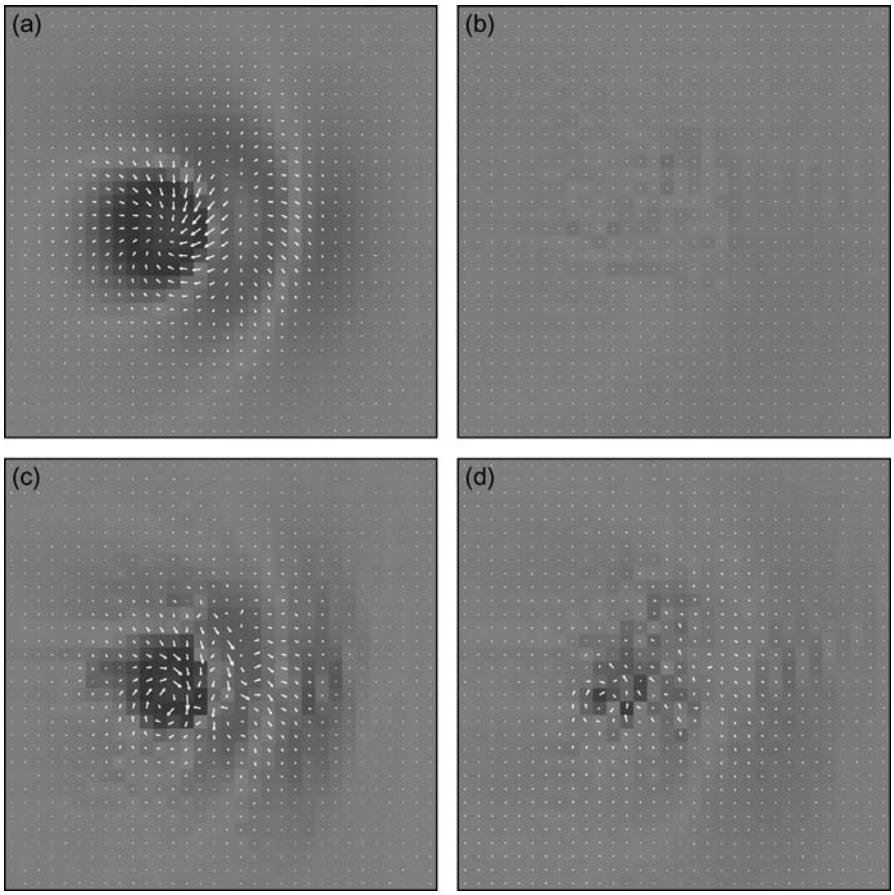

Figure 5. (a) The horizontal (vectors) and vertical (background image) components of the magnetic field in Case II for the central 32^2-pixel area; (b – d) Differences between the Wiegelmann solution and the input model for layers in a volume with height (z) normalized to range from 0 to 1, shown at $z = 0$, 0.125, 0.25, respectively, multiplied by 25 relative to the scaling for panel (a).

7. Discussion and Conclusions

In this study, we compare the relative merits of six existing methods for the computation of nonlinear force-free magnetic fields given the vector field on at least one boundary surface. The success of the methods is assessed by qualitatively comparing field line patterns and by quantitatively comparing five figures of merit for either vector differences or energy content. The figures of merit for vector errors (Equations (28) – (31)) result in essentially the same ordering of the models as does the visual inspection of the field line patterns. Metrics based on normalized differences between input and model field have the strongest differentiating power.

We find that the optimization method implemented in algorithms by Wiegelmann and by McTiernan are the most successful in modeling the field, particularly in the

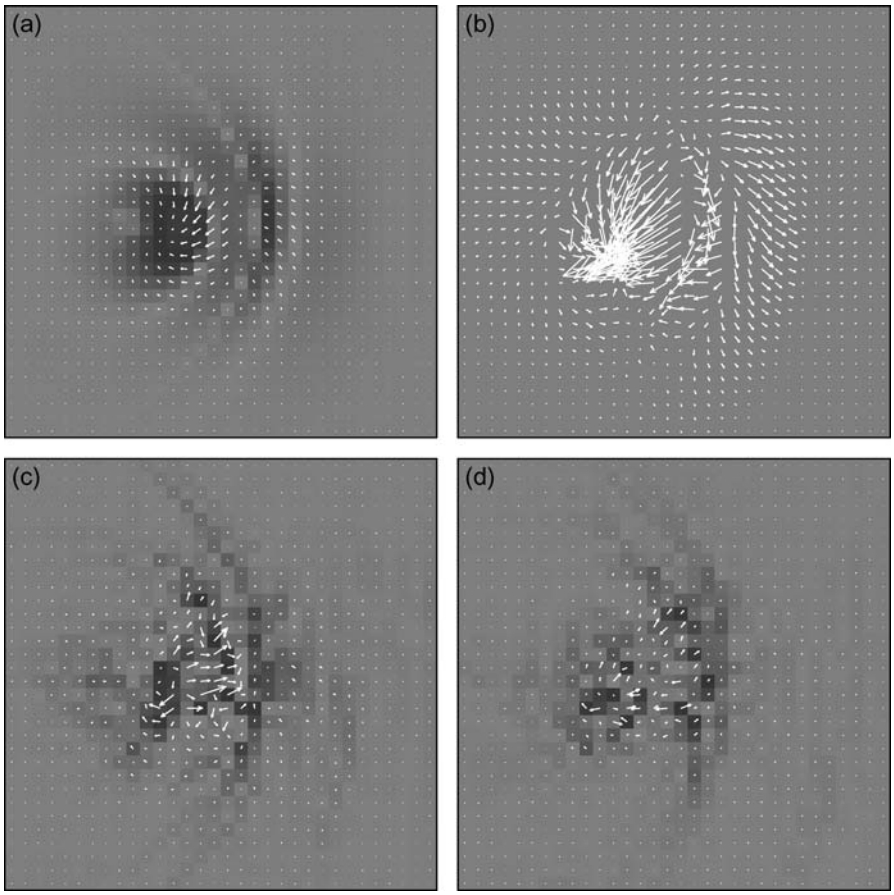

Figure 6. (a) The horizontal (vectors) and vertical (background image) components of the electrical current in Case II for the central 32 × 32-pixel area; (b – d) Differences between the Wiegelmann solution and the input model for layers in a volume with height (z) normalized to range from 0 to 1, shown at $z = 0, 0.125, 0.25$, respectively, multiplied by ten relative to the scaling for panel (a).

strong-field, strong-current regions in the central areas of the model volume. The NLFF vector fields in the outer domains of the volume depend sensitively on the details of the specified boundary conditions. Not surprisingly, the best agreement is found if the field outside of the model volume is incorporated as part of the model boundary, preferably in the form of vector-field or potential-field boundaries on the side and top surfaces, or at least as a potential field in a large area around the volume of interest.

The implementation of the boundary conditions turns out to be the most important limitation to successful field modeling for the models in our comparison. In this respect, we refer to the work of Amari, Boulmezaoud, and Aly (2005) who developed two Grad – Rubin-like methods and applied these to the same test fields

that we use here. They specify the vector field on all six boundaries for the two fields that we model in Cases I and II. We can thus directly compare the results only for Case I, but these show metrics that are even somewhat better than those for the Wiegelmann solution. We thus conclude that it is not the Grad – Rubin-based method, but rather the way in which the boundary conditions are implemented, that causes the Régnier model to perform relatively poorly.

For input field **B** and modeled field **b**, the best algorithm yields an average relative vector error $E_{\mathrm{N}} = \langle|\mathbf{B}-\mathbf{b}|\rangle/\langle|\mathbf{B}|\rangle$ of only 0.02 for Case I when all sides are specified and 0.14 for Case II where only the lower boundary is specified. Because these algorithms match the model vector field well, they also reproduce the total energy in the field, to within 4% for the best solutions for Case II for which only the lower boundary was provided. The successful determination of the total energy contained in a volume relative to the potential field is important when attempting to estimate the free energy in real solar cases.

It is also important to know where such free energy resides, or where the strongest electrical currents run. The best models map these currents quite well, and measure the energy in the magnetic field configuration to within a few percent.

The algorithms iterate at speeds that differ by a factor of one million per iteration step. The fastest-converging, best-performing model for these analytical test cases is the Wheatland, Sturrock, and Roumeliotis (2000) optimization algorithm as implemented by Wiegelmann, taking 15 CPU minutes (see Table I for the resource details). The Wiegelmann and McTiernan models are comparable in their success in recovering the NLFF vector magnetic field, but the Wiegelmann code converges some 50× faster having been optimized in C rather than IDL.

Even the fastest of these algorithms presents us with significant problems when the resolution is increased, however, as one would hope to do once routine high-resolution vector-magnetic field measurements become available from SOLIS and *Solar-B*. A computation of a relatively small volume of 512^3 pixels (significantly under-utilizing the observational capabilities of the 2048×4096 *Solar-B*/FPP detector or the 4096×4096 SDO/HMI detector), for example, would take approximately 8000 hours of CPU time. For routine analysis of multiple daily measurements that could only be done on a system of at least 1000 parallel processors. The task ahead must consequently focus both on the best possible use of observable boundary conditions as well as on the development of significantly faster methods. We plan to face these tasks by testing the methods on real solar vector magnetograms and comparing the results with observed coronal configurations, as well as by focusing on code parallelization and optimization.

Acknowledgements

We thank Dr. Yan for his help in running and documenting the boundary-integral method, Dr. Amari for coordinating his study with ours by adopting the same test

cases and metrics that we developed, and the referee for detailed comments which significantly improved the readability of the manuscript. This study was supported by Lockheed Martin Independent Research funds. The work of T. Wiegelmann was supported by DLR-grant 50 OC 0007 and a JSPS visitor grant at the National Astronomical Observatory in Tokyo. M. Wheatland acknowledges the support of an Australian Research Council QE II Fellowship. G. Valori was supported by DFG grant HO 1424/9-1.

References

Aly, J.J.: 1989, *Solar Phys.* **120**, 19.
Amari, T., Boulmezaoud, T.Z., and Aly, J.J.: 2005, *Astron. Astrophys.*, in press.
Amari, T., Boulmezaoud, T.Z., and Mikić, Z.: 2006, *Astron. Astrophys.* **446**, 691.
Amari, T., Aly, J.J., Luciani, J.F., Boulmezaoud, T.Z., and Mikić, Z.: 1997, *Solar Phys.* **174**, 129.
Bleybel, A., Amari, T., van Driel-Gesztelyi, L., and Leka, K.D.: 2002, *Astron. Astrophys.* **395**, 685.
Chiu, Y.T. and Hilton, H.H.: 1977, *Astrophys. J.* **212**, 873.
Dedner, A., Kemm, F., Kröner, D., Munz, T., and Wesenberg, M.: 2002, *J. Comp. Phys.* **175**, 645.
Gary, G.A.: 1989, *Astrophys. J. Suppl. Ser.* **69**, 323.
Gary, G.A.: 2001, *Solar Phys.* **203**, 71.
Grad, H. and Rubin, H.: 1958, in *Proceedings of the 2nd International Confenrence on Peaceful Uses of Atomic Energy, Vol. 31*, United Nations, Geneva, 190.
Leka, K.D. and Skumanich, A.: 1999, *Solar Phys.* **188**, 3.
Li, Z., Yan, Y., and Song, G.: 2004, *Mon. Not. Roy. Astron. Soc.* **347**, 1255.
Liu, Y., Zhao, X.P., Hoeksema, J.T., Scherrer, P.H., Wang, J., and Yan, Y.: 2002, *Solar Phys.* **206**, 333.
Low, B.C. and Lou, Y.Q.: 1990, *Astrophys. J.* **352**, 343.
Marder, B.: 1987, *J. Comp. Phys.* **131**, 48.
McClymont, A.N., Jiao, L., and Mikić, Z.: 1997, *Solar Phys.* **174**, 191.
McClymont, A.N. and Mikić, Z.: 1994, *Astrophys. J.* **422** 899.
Metcalf, T.R.: 1994, *Solar Phys.* **155**, 235.
Metcalf, T.R., Jiao, L., McClymont, A.N., Alexander, N., Canfield, R.C., and Uitenbroek, H.: 1995, *Astrophys. J.* **439**, 474.
Régnier, S. and Amari, T.: 2004, *Astron. Astrophys.* **425**, 345.
Régnier, S., Amari, T., and Kersalé, E.: 2002, *Astron. Astrophys.* **392**, 1119.
Roumeliotis, G.: 1996, *Astrophys. J.* **473**, 1095.
Sakurai, T.: 1981, *Solar Phys.* **69**, 343.
Schrijver, C.J., De Rosa, M.L., Title, A.M., and Metcalf, T.R.: 2005, *Astrophys. J.* **628**, 501.
Schrijver, C.J., Title, A.M., Berger, T.E., Fletcher, L., Hurlburt, N.E., Nightingale, R., Shine, R.A., Tarbell, T.D., Wolfson, J., Golub, L., Bookbinder, J.A., DeLuca, E.E., McMullen, R.A., Warren, H.P., Kankelborg, C.C., Handy, B.N., and De Pontieu, B.: 1999, *Solar Phys.* **187**, 261.
Seehafer, N.: 1978, *Solar Phys.* **58**, 215.
Valori, G., Kliem, B., and Keppens, R.: 2005, *Astron. Astrophys.* **433**, 335.
Wang, H., Yan, Y., Sakurai, T., and Zhang, M.: 2000, *Solar Phys.* **197**, 263.
Wheatland, M.S.: 2004, *Solar Phys.* **222**, 247.
Wheatland, M.S., Sturrock, P.A., and Roumeliotis, G.: 2000, *Astrophys. J.* **540**, 1150.
Wiegelmann, T.: 2004, *Solar Phys.* **219**, 87.
Wiegelmann, T. and Inhester, B.: 2003, *Solar Phys.* **214**, 287.
Wiegelmann, T., Inhester, B., and Sakurai, T.: 2005, *Solar Phys.*, in press.

Wiegelmann, T., Inhester, B., Lagg, A., and Solanki, S.K.: 2005a, *Solar Phys.* **228**, 67.
Wiegelmann, T., Lagg, A., Solanki, S. K., Inhester, B., and Woch, J.: 2005b, *Astron. Astrophys.* **433**, 701.
Yan, Y. and Li, Y.: 2006, *Astrophys. J.* **638**, 1162.
Yan, Y. and Liu, Y.: 1995, *Publ. Beijing Astron. Obs.* **27**, 11.
Yan, Y. and Sakurai, T.: 1997, *Solar Phys.* **174**, 65.
Yan, Y., Deng, Y., Karlický, M., Fu, Q., Wang, S., and Liu, Y.: 2001, *Astrophys. J.* **551**, L115.
Yan, Y. and Sakurai, T.: 2000, *Solar Phys.* **195**, 89.
Yang, W.H., Sturrock, P.A., and Antiochos, S.K.: 1986, *Astrophys. J.* **309**, 383.